Halogen-Bonded BODIPY Frameworks with Tunable Optical Features

Emrah Özcan[1,2] Burcu Dedeoglu[1], Yuri Chumakov[3], Ayşe Gül Gürek[1], Yunus Zorlu[1]*, Bünyemin Coşut[1]*, Mehmet Menaf Ayhan[1]*

[1] Department of Chemistry, Gebze Technical University, Gebze, Kocaeli, Turkey

[2] Institute of Physics, Faculty of Science, University of South Bohemia, Branišovská 1760, 370 05, České Budějovice, Czech Republic

[3] Department of Physics, Gebze Technical University, Gebze, Kocaeli, Turkey

Abstract

The ability to tune optical features of BODIPY materials is essential for their photo-related application. However, it is challenging to efficiently tune the crystal packing of BODIPY derivatives because of their complex nature. In this study, such control of BODIPY supramolecular assemblies was achieved by designing a BODIPY containing a halogen bond (XB) acceptor (–NO2) and donor (I, Br) to mediate halogen bonding interactions. The mono halogenated 2 and 4 was unable to form XB, whereas 3 and 5 formed isostructural mono-coordinate motif 3, 5-I (1D tubular structure) and symmetric bifurcated motif 5-II (1D zig-zag chains structure) via N-O···I,Br XB interactions. The results show that the dispersion and electrostatic component are the major source of 3, 5-I and 5-II XB formations. The XB interaction between –NO2 and X (I, Br) promote singlet-to-triplet intersystem crossing and triplet-to-singlet reverse intersystem crossing due to delocalization of oxygen electrons partially onto the Br and I. Then this interaction leads to unexpected fluorescence enhancement of 5-II. Finally, the indirect optical band gaps of the 3, 5-I and 5-II were able to be tuned in the range of 1.9–2.50 eV via XB driven crystal packings.

Introduction

Boron dipyrromethene (BODIPY) is one of the most actively studied a class of versatile organic fluorophores in the field of fluorescent imaging and sensing[1,2], solar cells[3], photodynamic therapy[4,5], organic semiconductors[6] and organic light-emitting diodes (OLED)[7] thanks to their ease of synthesis, excellent photostability and tunability of their photophysical properties. Most of the photo-related applications exploit photophysical properties of the BODIPY derivatives in diluted solution because, in contrast to their excellent luminescence in a solution, BODIPY derivatives like most of organic chromophores usually suffer from aggregation-caused quenching (ACQ)[8,9] and exhibit weak fluorescence in the aggregate state which greatly limits their applications in solid-state.

In the past decade, significant effort has been made to prevent ACQ effects in order to preserve or even improve excellent optical monomer features of BODIPY derivatives in the solid state. Most current strategies to tune solid-state optical behaviors of BODIPY, focus on decorating BODIPY cores with bulky groups to increase the intermolecular stacking distance which has the shortcoming of requiring elaborate structural design and considerable synthetic effort.[10,11] A novel approach has recently emerged for directing the optical features of fluorophore molecules in the solid state, which relies on careful control of the non-covalent interactions that lead to the assembly of monomers into the final aggregation or crystallization state.[12–14]

However, despite these efforts, this approach is still largely based on trial and error and not targeted design, due to the complex nature of structure–property relationship. Therefore, understanding the structure-property relationship is essential to obtain new materials with desired optical features. Polymorphism, is the capability of a compound to adopt multiple packing motifs in the solid, provide an ideal platform to explore essential structure-property relationship by excluding the effect of chemical modification.[15,16] It is known that the nature of non-covalent interactions between neighboring molecules have profound effects not only on crystal packing, but also on optical properties (e.g. emission, optical bad gap) of solid-state materials as much as chemical structure.[17,18] Therefore, it is of vital importance to understand the non-covalent interactions between the molecular components and their role in modulating the optical properties of the fluorophore.

These intermolecular interactions include hydrogen bonding (HB), halogen bonding (XB), electrostatic, dipole–dipole and van der Waals interactions. Among these interactions, halogen bonding (XB) has emerged as an excellent tailoring tool for supramolecular assemblies of varies photo-functional materials. XB is known for its highly tunable properties such as directionality, hydrophobicity, strength and length.[19–23] XB can be defined as an attractive interaction between a positive electrostatic region present on a halogen atom and an electron donor such as Lewis base, anion or radical.[24] The formation of halogen bonds results primarily from electrostatic force. However, polarization, charge transfer, and dispersion forces also play a significant role.[24,25] Contributions of these noncovalent interactions towards XB often depends on the individual interacting compounds.

Another distinctive feature of XBs is that interaction of the large size of bond-donating atoms (bromine, iodine) with oxygen can promote efficient fluorescence or phosphorescence emission in the chromophore by promoting electron delocalization, which allows to harvest singlet and triplet excitations simultaneously.[26–30] These combined features make XBs an excellent tailoring tool for rational design and crystal engineering to effectively tune optical features.[31]

Because of complex nature of halogen bonding, most crystal engineering designs are predominantly based on small molecular structures. Therefore, it offers a great challenge to efficiently drive crystal packing of a complex structure such as BODIPY to tune optical properties via halogen bonding with other cooperative non-covalent interaction.

In our molecular design, **I** and **Br** were chosen as XB donors since they are capable of forming the strongest XBs and promote emission in the organic chromophore.[32,33] The **-NO_2** functional group was chosen as XB acceptor group due to three advantages. First, its strong electron-withdrawing ability increases the positive electrostatic potential of the σ-hole on halogens. Second, **-NO_2** group is a strong Lewis base and thus can form strong XB. Finally, **-NO_2** group is known to be involved in three different motifs; (**I**) mono-coordinate motif, (**II**) asymmetric bifurcated motif and (**III**) symmetric bifurcated motif which increases the probability of obtaining polymorph crystal packing (Fig.1).[34]

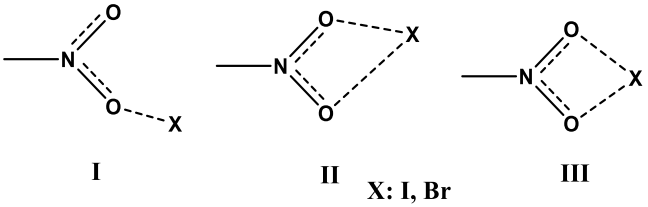

Figure 1. The possible X/NO_2-synthon geometries.

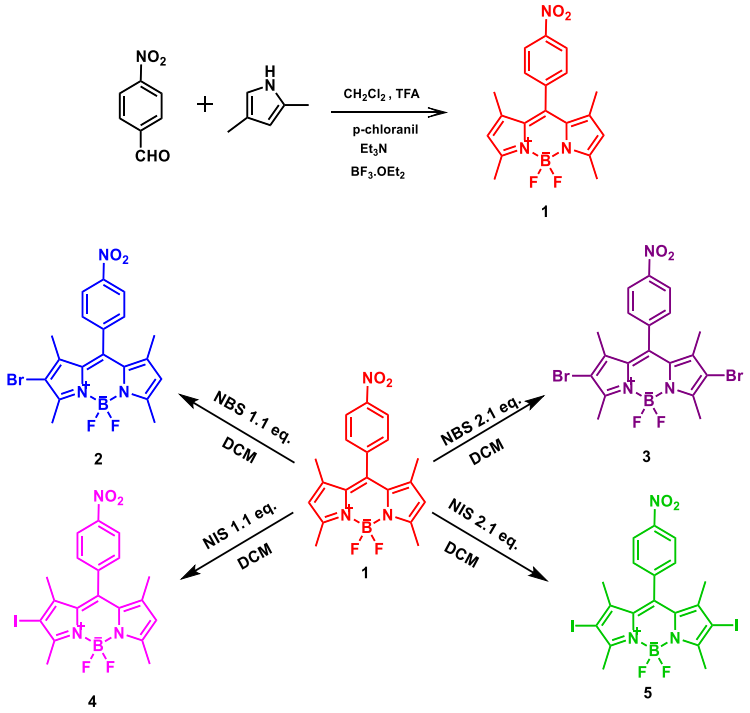

Scheme 1. Synthetic pathway of compounds **1- 5**.

Consequently, the following series of BODIPY **(2-5)** derivatives were prepared based on the design criteria described (Scheme 1). Until now, to the best of our knowledge, no other study has been devoted to BODIPY assemblies by XB interactions and rational crystal design with the aim to tune optical properties in solid state. Various experimental (X-ray diffraction, FT-IR, UV-Vis, Reflectance (DRS) and Fluorescence spectroscopy) and detailed theoretical analyses including MEPS (Molecular electrostatic potential surfaces)[35],tThe LOLIPOP (Localized Orbital Locator Integrated Pi Over Plane)[36], SAPT (Symmetry-adapted Perturbation Theory) [37–39] and Hirshfeld Surface have been used to elucidate both the interaction mechanism of halogen bonding and structure-property relationship in term of optical properties of BODIPY dyes in solid-state. The present work demonstrates the first successful efforts to utilize the halogen bonding driven force for crystal engineering of BODIPY supramolecular assemblies in solid-state, which we believe will be widely used for future design and application of optical functional materials with predictable and modulated optical properties.

Results and discussion

Materials and methods

All chemicals and solvents were purchased from Sigma Aldrich and TCI Chemicals used as supplied without further purification unless stated otherwise. NMR spectra were recorded on a Bruker 400 spectrometer (^{1}H, 500 MHz; ^{13}C, 125 MHz). MALDI-TOF was performed on a Bruker Microflex LT MALDI-TOF-MS Instrument. Electronic absorption spectra of the compounds in the UV-Vis region were measured with a Shimadzu 2101 UV-Vis spectrophotometer (Tokyo, Japan). Varian Eclipse spectrofluorometer (Melbourne, Australia) using 1 cm path length cuvettes was used for determination of fluorescence excitation and emission spectra at room temperature. The diffuse reflectance spectra (DRS) were recorded with ISR-2600-Plus Shimadzu spectrophotometer. Fourier-Transform Infrared (FTIR) spectra was recorded by Perkin Elmer Spectrum 100 Optical FT-IR Spectrometer. Confocal imaging was performed by Zeiss LSM880 Airyscan Confocal Microscopy (Carl Zeiss, Germany) with Plan-Apochromat 40X/1.4 Oil DIC M27. The optical texture observation was performed by using a polarized optical microscope (Leitz Wetzlar Orthoplan-pol). Solid-state Fluorescent Spectra (SFS) were collected by a Hitachi F-7000 fluorescence spectrophotometer that has a 650-0161 solid sample holder.

Synthetic procedures

The compounds **1**[40], **2** and **3**[41], **4** and **5**[42] were synthesized following previously reported procedures with some improving modification. The details of experimental procedures and all spectral data are given in the ESI.

Crystallization conditions

For each compound (**2-5**), the solid was dissolved in a minimum amount (4 mL) of solvent and then left in a vial for slow evaporation in order to obtain crystals suitable for single crystal X-ray diffraction analysis. Crystallization was performed with both polar (dichloromethane, tetrahydrofuran, acetone, acetonitrile) and apolar (benzene, chloroform, 1,4-dioxane) solvents for each compound. While compound **2,3,4,5-I** crystals remained dark red, a new polymorph **5-II** was found through crystallization of **5** with acetonitrile (Fig.S16).

X-ray Crystallography

Data was obtained with Bruker APEX II QUAZAR three-circle diffractometer. Indexing was performed using APEX2[43]. Data integration and reduction was carried out with SAINT[44]. Absorption correction was performed by multi-scan method implemented in SADABS[45]. The structure was solved using SHELXT[46] and then refined by full-matrix least-squares refinements on F^2 using the SHELXL[46] in Olex2 Software Package[47]. Aromatic and aliphatic C-bound H atoms were positioned geometrically and refined using a riding mode. Crystallographic data and refinement details of the data collection for BODIPY derivatives are in Table S1. Crystal structure validations, geometrical calculations and crystal packing analysis were performed using Platon software[48]. The hydrogen bonds (D-H···A) were described by following parameters: d(D···A) < R(D)+R(A)+0.5 Å, d(H···A) < R(H)+R(A)-0.12 Å, angle D-H···A > 100º , where R(I) and R(J) are the van der Waals radii of i-and j-th atoms[49]. The molecular drawings were carried out with Mercury CSD (version 3.5.1) program[50]. The Crystallographic Information *Files* with CCDC reference numbers 2002684-2002688 have been deposited within the Cambridge Crystallographic Data Center *via* www.ccdc.cam.ac.uk/deposit

Computational Methodology

Molecular electrostatic potential surfaces were calculated with the density functional M06-2X as implemented in Gaussian09[35]. For iodine and bromine, DGDZVP and for the rest of the atoms 6–31+G(d,p) basis sets were used. The LOLIPOP (Localized Orbital Locator Integrated Pi Over Plane)[36] and HOMA (Harmonic Oscillator Model of Aromaticity)[51] aromaticity indexes were performed with the help of Multiwfn software (v. 3.3.5)[52], using the wave functions generated by the Gaussian 09. LOLIPOP is defined as definite integral of Localized Orbital Locator (the LOL purely contributed by π-orbitals), which is a function of the kinetic energy density. LOL offers an intuitive depiction of π-bonds and detailed

information on the nature and location of electron pairs[53,54]. The integration was made in a cylindrical region perpendicular to the molecular plane and from a distance of 0.5 Å away from this plane.

The analysis of non-covalent interactions was carried out by employing the symmetry-adapted perturbation theory (SAPT) which separates out the physical meaningful components of given interaction such as electrostatic ($\mathbf{E_{elst}}$), exchange-repulsion ($\mathbf{E_{exch}}$), induction ($\mathbf{E_{ind}}$), and dispersion ($\mathbf{E_{disp}}$).[37–39] To achieve this decomposition, the Hamiltonian is partitioned into monomeric Fock operators, *Møller–Plesset* fluctuation operators and intermolecular interaction operators. All SAPT calculations were performed with the Psi4 program using density fitting at the sSAPT0/jun-cc-pVDZ level.[55]

Analysis of studied structures

The solid-state structures of compounds **2**, **3**, **4**, **5-I, 5-II** (Fig. S17) were studied by single-crystal X-ray analysis for monomers and crystal packing in order to gain more insight into the molecular structure, packing, and intermolecular interactions with regards to structure-property relationships.

In the ground state of **3**,**4**,**5-I** compounds the dihedral angle between two halves of central ring ranges from 4.6 to 6.8º while for compounds **2** and **5-II** it equal to 3.5 and 3.3º respectively. However, the maximal values of the torsion angle BNCC in the central ring of **2-5-I** lie in the interval 4.6 ÷ 8.9º whereas for **5-II** it is 0.9º. The deviations of B atoms from BODIPY core in **2 - 5-I** are in interval 0.104 ÷ 0.148 Å while in **5-II** this value is equal to 0.034 Å (Fig. 2), that indicates a geometry deformation of BODIPY core in **2-5-I** compared to **5-II**. The inter-ring dihedral angles between the meso-phenyl group and the boron-dipyrromethene plane are 79.58º for **2**, 74.67º for **3**, 78.59º for **4**, 74.53º for **5-I**, 87.47º for **5-II**, that is steric hindrance of *β*-pyrrole methyl substituents[40] (Fig. 2).

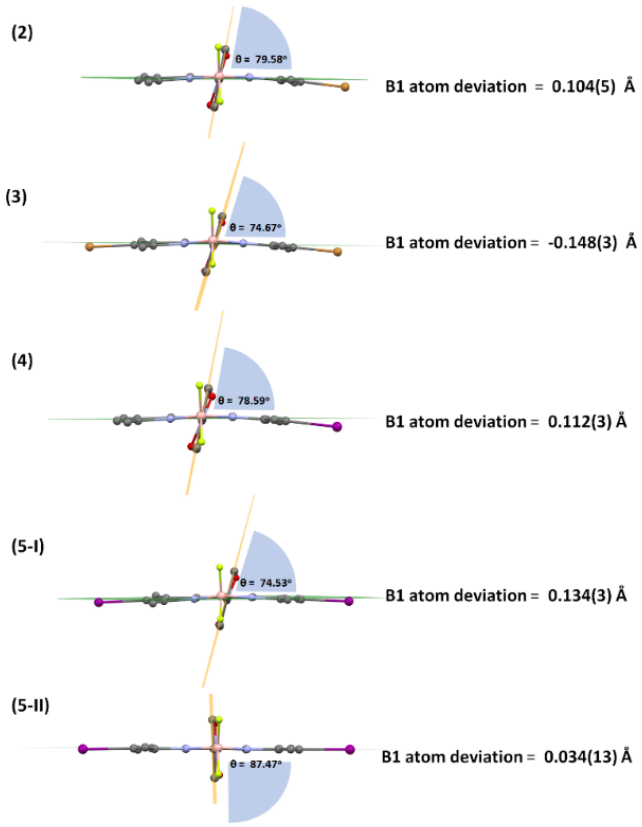

Figure 2. Perspective view of the crystal structures of **2**, **3**, **4**, **5-I** and **5-II** showing the corresponding dihedral angles (between meso-phenyl and BODIPY π-backbone) and deviations of B atoms from C9N2B core.

In solid state of compound **1**, the molecules are joined into chains *via* C-H···O hydrogen bonds to form 1D chain structure, which are further connected to each other by C-H···F hydrogen bonding interactions (Fig. S18). The introduction of one halogen atom (**Br, I**) into **1** has led to the formation of isostructural crystal packing of **2** and **4** which form dimers through CH···F hydrogen bonds (Fig. 3, Table S2). As shown in Fig. 3A and 3B, the molecular dimers in **2** and **4** are extended into a 1D chains *via* weak CH···F hydrogen bonding along the *a*-axis. These chains are linked by NO···π interactions (d(O···π) ~ 3.780 Å) between the oxygen atoms of *p*-NO_2 group and benzene centroid along the *c*-axis (Fig. 3C and 3D). Also, the F···π (d(F···π) ~ 3.595 Å) interactions between the halogen atoms and the aromatic planes of BODIPY were observed in the structure of **2** and **4** (Fig. 3E and 3F). However, despite the presence of strong XB donor (**Br, I**) and XB acceptor (**-NO_2**) in both structures (**2** and **4**), halogen bonding has not occurred due to competition of other non-covalent interactions

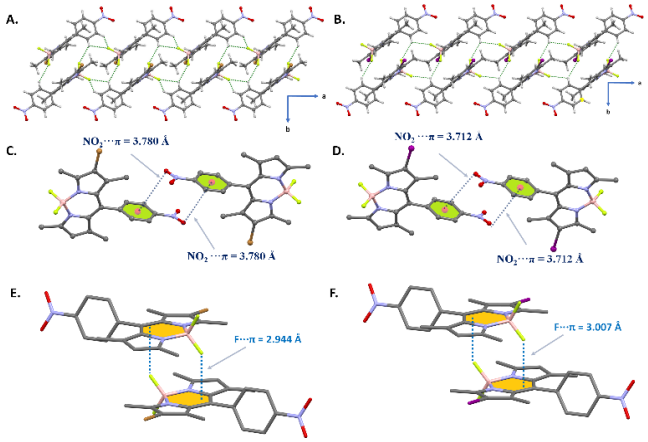

Figure 3. The intermolecular C─H···F HBs (A, B), NO_2···π (C, D), and F···π (E, F) contacts compound **2** (right side) and **4** (left side).

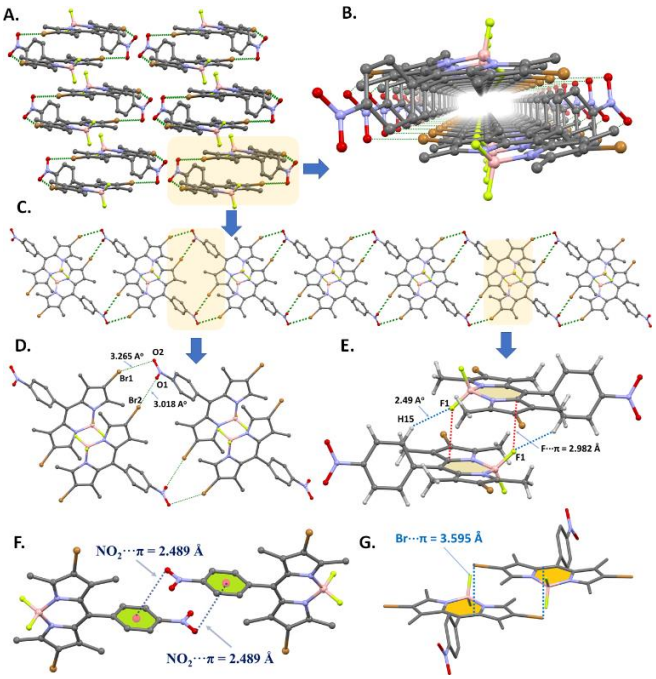

Figure 4. (**A**) The unit cell packing of **3**. (**B**) The front-view illustration of tubular architecture connected by Br1···O2 and Br2···O1 halogen bonds. (**C**) and (**D**) side-view illustration of 1D nanotube, showing the Br···O XB distances. (**E**) Perspective view of intermolecular C─H···F hydrogen bonds and F···π_{BODIPY} interactions stabilizing 1D tubular structure. (**F**) The intermolecular NO_2···π contacts in anti-parallel arranged compound (**3**). (**G**) The intermolecular Br•••π_{BODIPY} contacts in anti-parallel arranged compound (**3**).

The addition of two halogen atoms (**Br, I**) into **1** has led to the formation of isostructural crystal packing of **3** and **5-I** which form dimers through cooperative CH···F HBs and F···π interactions (Fig. 3E, 4E). These dimers extend to well-defined one dimensional (1D) tubular architectures (Fig. 4B, 4C, 5B, 5C) along [110] direction, through similar mono-coordinate motif XBs (C-Br···O(nitro), *d*(Br···O) = 3.2646(18) Å and 3.0177(18) Å in Fig. 4D) for **3** and C-I···O(nitro) (*d*(I···O) = 3.484(2) Å and 3.193(3) Å in Fig.5D) for **5-I**). Moreover, the self-assembled 1D tubular structure of **3** and **5-I** are further stabilized by cooperative weak intermolecular interactions CH···F (d(H···F) = 2.484 Å for **3** and d(H···F) 2.625 Å for **5-I**, Fig. 4E, 5E), F···π_{BODIPY} (3-2.982 Å and **5-I**-2.970 Å), NO···π (**3**-**5-I**(d(O···π) ~ 2.489 Å) and X(Br, I)···π (**3**-(d(Br···π) ~ 3.595 Å and **5-I**-(d(I···π) ~ 3.663 Å), Fig. 4G, 5G).

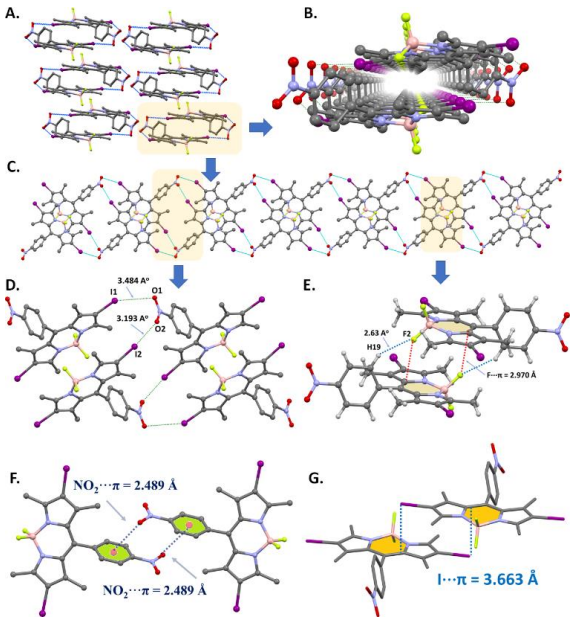

Figure 5. (**A**) The unit cell packing of **5-I**. (**B**) The front-view illustration of 1D tubular structure linked by I2···O2 and I1···O1 halogens. (**C**) and (**D**) side-view illustration of 1D tubular structure, showing the Br···O XB distances. (**E**) Perspective view of intermolecular C─H···F hydrogen bonds and F···π_{BODIPY} interactions stabilizing tubular structure. (**F**) The intermolecular NO_2···π contacts in anti-parallel arranged compound (**5-I**). (G) The intermolecular I···π_{BODIPY} contacts in anti-parallel arranged compound (**5-I**).

During our crystallization efforts, **5** has adopted two polymorph crystal structures depending on the solvent polarity. It forms **5-I** crystal packing in apolar and moderately polar solvents, whereas it forms **5-II** in polar acetonitrile solvent. In the crystal of **5-II**, the molecules are joined by the nearly symmetrical bifurcated C-I···O(nitro) (*d*(I···O) = 3.429(12) Å and 3.474(12) Å) XBs forming the 1D zig zag chains along the *b*-axis (Fig. 6D)[56–58]. These chains are further linked by 3D supramolecular network of the CH···F and CH···O HBs (Figure 6A, 6B, 6C, Table S2).

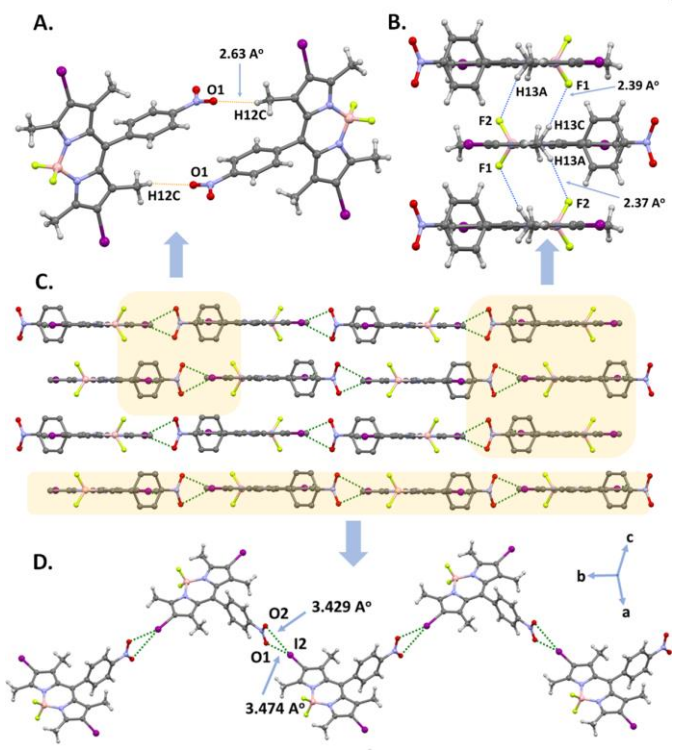

Figure 6. (**A, B**) Fragments of the structure showing the formation of C─H···O and C─H···F hydrogen bonds between 1D zig zag chains. (**C, D**) Perspective view of 2D layered crystal network of **5-II** and formation of bifurcated I2···O2 and I1···O1 XBs.

Analysis of non-covalent interactions.

Theoretical studies are important to understand noncovalent interactions and their properties. Halogen bonds form as a result of noncovalent interaction between σ-hole, specific region of positive electrostatic potential located at the outer tip of the halogen, and an electron-rich atom (Lewis base) in a highly directional way. In general, the magnitude of the σ-hole depends on three factors, the electronegativity of the halogen atom, its polarizability, and the electron withdrawing power of the substituted group.[23,59] The strengths of XBs correlate with the magnitudes of the positive and negative electrostatic potentials of the σ-hole and the negative site. The nature of halogen bond formation is frequently assigned to be electrostatic, however polarization, charge transfer, and dispersion forces can also be the dominant stabilizing factors in some cases.

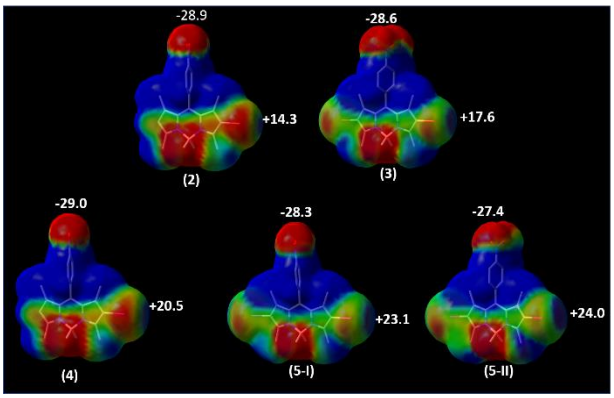

Figure 7. Electrostatic potentials mapped on the molecular surfaces of **2 – 5-I** and **5-II**.

The σ-hole interactions of **2, 3, 4, 5-I** and **5-II** have been investigated and visualized using the electrostatic potential maps[59,60] and results are displayed in Fig. 7 along with the corresponding electrostatic potential values. As expected, the results show that positive potential surrounding the aromatic ring of nitro benzene and a negative potential on the nitro group and fluor atom of BF_2 moity. It is evident that a positive potential exists on the outer tip of the halogen atom (σ-hole) in all BODIPY derivatives. The magnitude of positive electrostatic potential of iodine σ-hole is much larger compared to bromine σ-hole due to its lower electronegativity and higher polarizability. Furthermore, the larger positive potential of the σ-hole is observed when the second halogen atom is introduced to BODIPY core for **3** and **5**. Unexpectedly, despite all BODIPY derivatives possessing **-NO_2** as Lewis base with large negative potential and **X (Br, I)** as Lewis acid with large positive potential groups, only two halogenated structures (**3, 5**) can form XBs (Fig. 8). Interestingly, with the formation of XB dimers, electrostatic potential maps of **3** and **5-I** remained the same, whereas **5-II** has changed unevenly. The positive potential of **5-II's I-1** has decreased while **I-2** slightly increased. This new electrostatic potential distribution may explain why only **I-2** was able to join to formation of XB, whereas **I-1** unable to.

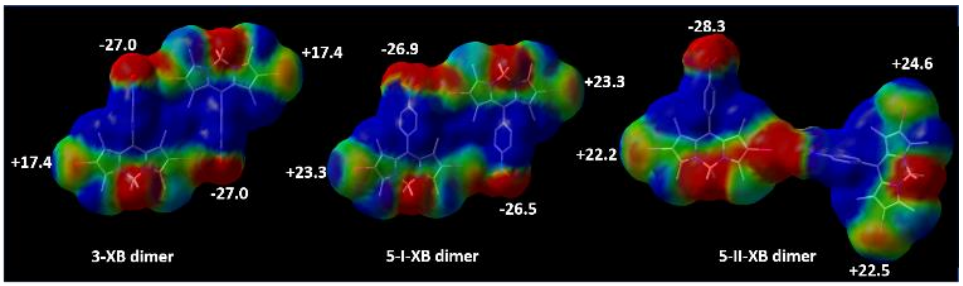

Figure 8. Electrostatic potentials mapped on the molecular surfaces of XB dimer of **3 – 5-I** and **5-II**.

Table 1. Halogen bond parameters **(**Å and °) in **3, 5-I** and **5-II**

D-X···O	Symmetry X···O-N	d(X···O) Å	D-X···O	
3				
C2-Br1···O2	-1+x, 1+y, z	3.2646(18)	152.64°	106.2°
C8-Br2···O1	2-x, 1-y, 1-z	3.0177(18)	172.85°	105.45°
5-I				
C8-I2···O2	-x, 1-y, 1-z	3.193(3)	166.82°	101.36°
C2-I1···O1	1+x, -1+y, z	3.484(2)	150.46°	106.03°
5-II				
C8-I2···O2	3/2-x, 1/2+y, 3/2-z	3.429(12)	164.25°	101.52°
C8-I2···O1	3/2-x, 1/2+y, 3/2-z	3.474(12)	160.01°	99.18°

For compounds **3, 5-I** and **5-II** the internuclear X···O distances are less than the sum of their vdW radii and the angles of D-X···O and X···O-N range in the intervals 150.46÷172.85° and 99.18÷106.2° respectively (Table 1). The deviation of X···O bond from collinearity with D−X may be attributed to the packing effects and nature of σ-hole.[61] Moreover, the mentioned angles for studied XB lie in wider intervals as compared with **3, 5-I** and **5-II** (142.6÷176.6° and 109.3÷106.2° respectively). The decomposition of the binding energies of studied compounds can give us insight into the nature of its non-covalent interactions. The SAPT procedure partitions the total attractive forces into electrostatic ($\mathbf{E_{elst}}$), induction ($\mathbf{E_{ind}}$) and dispersion ($\mathbf{E_{disp}}$), leaving the exchange as the repulsive ($\mathbf{E_{exch}}$) term. The intermolecular interaction energies ($\mathbf{E_{int}}$) were calculated for pairs of molecules forming the halogen bonds (Fig. 4D, 5D, 6D). The calculated attractive components $\mathbf{E_{elst}}$, $\mathbf{E_{ind}}$ and $\mathbf{E_{disp}}$ for all XB pairs provide sufficient stabilization to overcome the repulsive exchange component, therefore the resultant $\mathbf{E_{int}}$ values are negative (Table 2, S3).

Table 2. Summary of SAPT results (kcal/mol) of **3**, **4**, **5-I** and **5-II**.

	Compound	E_{elst}	E_{exch}	E_{ind}	E_{disp}	E_{int}
XB	**3(Br2···O)**	-4.641	11.049	-1.762	-9.024	**-4.377**
	3(Br1···O)	-1.264	2.187	-0.409	-2.495	**-1.980**
	5-I(I2···O2)	-5.134	12.623	-2.252	-12.302	**-7.065**
	5-I(I1···O1)	-1.587	2.121	-0.450	-2.870	**-2.787**
	5-II(I-O)	-2.243	3.368	-0.866	-2.608	**-2.348**

The halogen bonds in **3** and **5-I** (Fig. 4D, 5D) have different lengths d(Br···O) are shorter than d(I···O) (Table 1) and yet, the pairwise comparison of XBs in these compounds revealed that iodine-containing XBs are stronger than bromine-containing ones. The strength of bifurcated halogen bond ($\mathbf{E_{int}}$) in **5-II** is smaller than its polymorph **5-I,** because XB in **5-I** contains the contribution from F···π and F···H hydrogen bonds. Overall, the results show that the dispersion component is the major source of $\mathbf{E_{int}}$ for all XBs non-covalent interactions with the electrostatic component as close second.

Hirshfeld surface analysis

Although the number of reported BODIPY dyes and derivatives in Cambridge Structural Database[62] increased in recent years, polymorphic forms rarely received attention[63] and comparative structural and crystallographic characterizations are still required. Here, two polymorphic forms **(5-I** and **5-II)** were visually compared by Hirshfeld surface calculations (as indicated in SI) and 2D fingerprint plots in order to get a better insight into the intermolecular interactions (Fig. S19). It is evident from 2D fingerprint plots that Hirshfeld surfaces of **5-I** and **5-II** display slightly different intermolecular interactions in each crystal structure (Fig. S20) and have a remarkable different molecular conformation as shown by dihedral angles between the meso-phenyl group and the boron-dipyrromethene plane (Fig. 2). The highest contribution to the total Hirshfeld surface (Fig. 9A) is from H···H interactions, which comprise 33.0% and 31.7% of the total Hirshfeld surface for **5-I** and **5-II**. The Hirshfeld surfaces of **5-I** and **5-II** were mapped over d_{norm} range of -0.2 to 1.5 Å. with only 5.8% and 6.3% contribution from the C-I···O halogen bonding interactions shown as two distinctive spikes in Fig. 9B, respectively. The C-I···O interactions in **5-I** and **5-II** are not the only interactions between molecular blocks, but they play a key role in stabilizing the crystal structure as can be seen in Fig. 4 and 5. The Hirsfeld surface and two-dimensional fingerprint plots of other major supramolecular interactions (H···I, H···O, H···C, H···F) have comparatively been shown in Fig. S20.

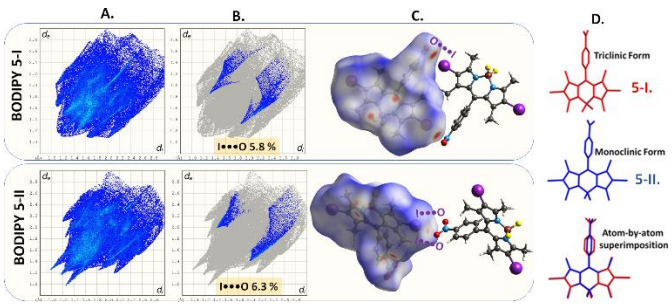

Figure 9. A. Full fingerprint plots of Hirshfeld surfaces (top: triclinic form (**5-I**), bottom: monoclinic form (**5-II**) **B.** Resolved fingerprint plots showing the percentage contribution of the I···O halogen bonding interactions to the total Hirshfeld surface area **C.** Hirshfeld surface representation of C-I···O XBs **D.** Capped-stick representations and atom-by-atom superimposition of two polymorphic structures (**5-I** and **5-II**).

Infrared Spectroscopy analysis

Among various experimental techniques, IR spectroscopy is a useful and effective method to study halogen bonding interactions at the molecular level.[64,65] Since halogen bonding formation occurs between **–NO₂** and **X(Br, I)** in our BODIPY structures, following $\upsilon_{N\text{-}O}$ asymmetric and symmetric stretching bands is the best way to determine interactions. The IR spectra of **2** and **4** show no change both in disordered and crystalline states (Fig. S22, S23). The IR spectra of **3-I**, **5-I,** and **5-II** derivatives are presented in Fig. 10. The peaks around 1510-1540 cm^{-1} are attributed to the $\upsilon_{N\text{-}O}$ asymmetric stretching band and those at 1300-1340 cm^{-1} are attributed to the $\upsilon_{N\text{-}O}$ symmetric stretching band, respectively. The halogen bond between **–NO₂** and **X(Br, I)** can form three motifs and the type of these motifs can be identified with $\upsilon_{N\text{-}O}$ asymmetric stretching band. Both **3-I** and **5-I** have mono-coordinate motif which attributed to double $\upsilon_{N\text{-}O}$ asymmetric stretching band around 1520-1538 cm^{-1} and 1516-1537 cm^{-1}, respectively. In contrast, **5-II** has a symmetric bifurcated motif which visible as one $\upsilon_{N\text{-}O}$ asymmetric stretching band at 1509 cm^{-1}. The formation XBs between the iodine and bromine to the **–NO₂** oxygen cause the shift in $\upsilon_{N\text{-}O}$ asymmetric stretching band, which indicate that **-N-O** bond is weakening. Since iodine form stronger XB than bromine, let to a bigger shift in $\upsilon_{N\text{-}O}$ stretching bands than bromine.

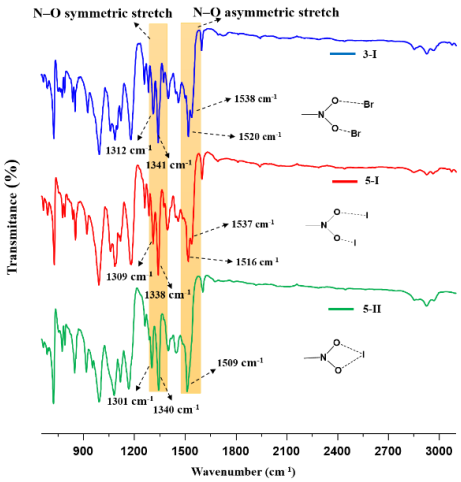

Figure 10. IR spectrum of **3-I**, **5-I and 5-II**'s crystalline forms. $\upsilon_{N\text{-}O}$ symmetric and asymmetric stretching band is highlighted.

Analysis of Photophysical Properties:

The optical and photophysical properties of **2-5** in solution and amorphous, in the absence of XBs, and crystalline states have been investigated by absorption/fluorescence spectroscopies and diffuse reflectance spectroscopy (DRS). Also, theoretical analyses of HOMA, LOLIPOP and molecular orbitals have been applied in order to gain more insight into the molecular structure, packing, and intermolecular interactions with regards to structure-property relationships.

The absorption spectra of **2–5** in solution possess a major absorption band (λ_{max}) in the region of 510-530 nm with the out-of-plane vibrionic features at 484/451 nm, which is a unique absorption profile of meso-aromatic BODIPY's π-π* transition ($S_0 \rightarrow S_1$) (Fig. S24)[66] . The absorption bands are bathochromically shifted for all BODIPY derivatives (**2-5**) with addition of halogen atoms. The shift is larger for the iodine derivatives (**4, 5**) compared to those bromines of (**2, 3**) (Fig. S25). The fluorescence spectra show very weak intensity in solution for **2-5** (Fig. S26). The weak emission is caused mostly by halogen atoms, which induce intersystem crossing via strong spin–orbit coupling between singlet and triplet states that known heavy-atom effect[67–71]. Additionally, delocalization toward meso-phenyl group in the BODIPY is known to lead to non-radiative decay which decrease the fluorescence efficiency.[72]

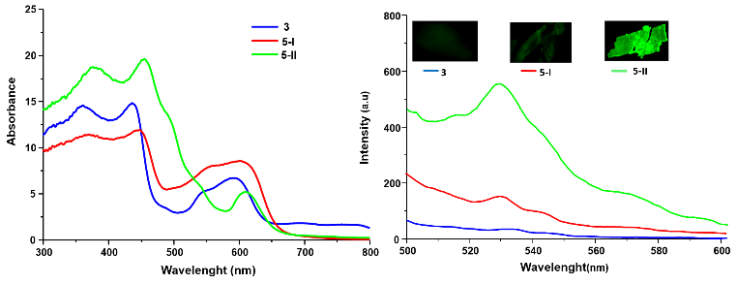

Figure 11. Absorption and fluorescence spectra of **3**, **5-I** and **5-II** in crystalline solid state.

The absorbance/emission measurements and fluorescence confocal images with variable excitation wavelengths of **2, 3, 4, 5-I** and **5-II** in solid state (disorders and crystalline) were subsequently measured and results are shown in Fig. 11, S27-30. The absorption bands are generally red shifted compared to the respective solution spectra. Interestingly, two polymorph structures **5** (**5-I** and **5-II)** exhibit different absorption profiles as seen in Fig. 11. The band corresponding to S_0-S_1 transition at 606 nm is remain nearly the same for both **5-I** and **5-II**, whereas S_0-S_2 transition band at 455 nm of **5-II** is red-shifted compared to **5-I** at 445 nm.

Surprisingly, despite all aforementioned emission quenching processes with addition of BODIPY's typical ACQ[73], crystalline **5-II** exhibits intense fluorescence emission, whereas crystalline **2, 3, 4** and **5-I** show weak emissions as expected. The nature of the fluorescence enhancement of **5-II** has been investigated experimentally and using theoretical analyses. These results indicate that several factors have contributed to this intense emission either through termination of quenching processes or by favoring emission pathway. The major contribution to emission comes from our unique XB design in crystalline. The strong halogen bonding between aromatic oxygen and large size of the bond-donating atoms (**Br**, **I**) lead to the delocalization of oxygen electrons partially onto the **Br** and **I**. This in turn, causes mixing of the singlet and triplet states of the excited chromophore to promote both singlet-to-triplet intersystem crossing (ISC) and triplet-to-singlet reverse intersystem crossing (rISC). When BODIPY **2-5** is in solution (or any disordered phase), where there is no halogen bonding, triplet generation is

dominant, which leads to triplet emission, and makes fluorescence emission inefficient due to internal heavy atom effect (Fig.12A). However, with halogen bonding formation between **Br**, **I** and oxygen in crystalline state, fluorescence emission is partially generated by triplet-to-singlet reverse intersystem crossing (rISC) (Fig.12B).

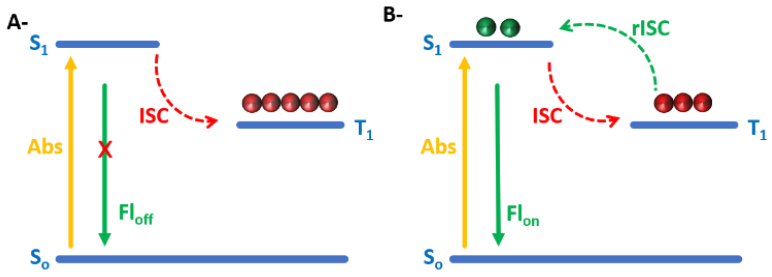

Figure 12. Simplified schematic representation of Photophysical mechanism of **A-** Fluorescence quenching via inter system crossing **B-** Fluorescence enhancement via reverse inter system crossing

The delocalization level between aromatic oxygen and bromine or iodine in **3**, **5-I** and **5-II** have been theoretically calculated by LOLIPOP analysis which measures π-delocalization ability of aromatic systems.[36] The smaller LOLIPOP value indicate lower π-delocalization (namely stronger π-depletion). The calculation of LOLIPOP has revealed that **5-II** possesses the maximal (7.692) value of this quantity while for **3** and **5-I** these values are 5.082 and 6.164, respectively. These results indicate that, XB has led to strong π-delocalization of BOPIPY core in order **5-II**>**5-I**>**3,** which is *in* agreement with the observed IR, absorption and fluorescence spectral features. Interestingly, the opposite is true for meso phenyl group, where **5-II** possess the minimal (0.132) value of LOLIPOP whereas for **3** and **5-I** these values are 2.944 and 1.976, respectively. This is likely related to different dihedral angles between meso-phenyl group and BODIPY core (Fig. 2). The additional theoretical analysis has also confirmed our results and the details are given in the ESI (Table S4 and S5).

Furthermore, the frontier molecular orbitals have been analyzed and the orbitals are depicted in Fig.13. The electron density of highest occupied molecular orbital (HOMO) distributes mostly over the BODIPY core for **3, 5-I** and **5-II.** However, the electron density is shifted towards meso-phenyl for the lowest unoccupied molecular orbital (LUMO) of **3** and **5-I** but almost completely localized on the BODIPY core for **5-II** (Fig. 13).

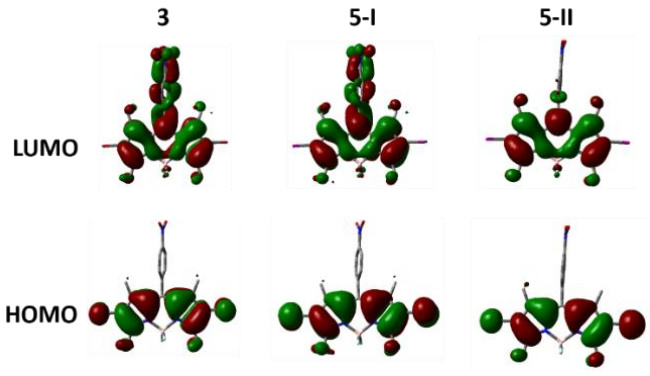

Figure 13. Molecular orbital plots of the HOMOs and LUMOs of **3**, **5-I** and **5-II**.

Optical Band gap measurements:

The optical band gaps of **3, 5-I** and **5-II** in solution, amorphous, in the absence of halogen bonding, and crystalline states have been investigated with diffuse reflectance spectroscopy (DRS) (Fig. S29) using the relational expression proposed by Tauc[74,75], Davis, and Mott[76] and calculation details are given in SI.

The DRS and Tauc plots for **3**, **5-I** and **5-II** in crystalline states are shown in Figure 14. The Tauc plot derived from first jump in the spectrum yields a narrow band gap at ca. 1.73-1.78 eV corresponding to the S0-S1 transition band of BODIPY core at 606-592 nm. The second jump in the spectrum yields a narrow band gap of 1.90 eV for **5-II**, 2.30 eV for **5-I** and 2.44 eV for **3,** which corresponds to the S_0-S_2 of BODIPY core at 455, 445 and 435 nm, respectively. The band gap of crystalline **5-II** decreases considerably compared to its disorder states (solution, amorphous), whereas band gap of crystalline **3** and **5-I** either increase or remain the same (Fig. S30-33, Table S6). This tunability of the optical band gap of BODIPY derivatives is mainly attributed to the extension level of conjugation via **N-O···I, Br** halogen bonding interactions. In addition, other factors, such as distortion of structure, layer thickness and other non-covalent interactions, will have an important impact on the band gaps of materials. Our data shows that band gaps of the BODIPY derivatives can be tuned in the range **1.90–2.50** eV by controlling crystal packing via halogen bonding.

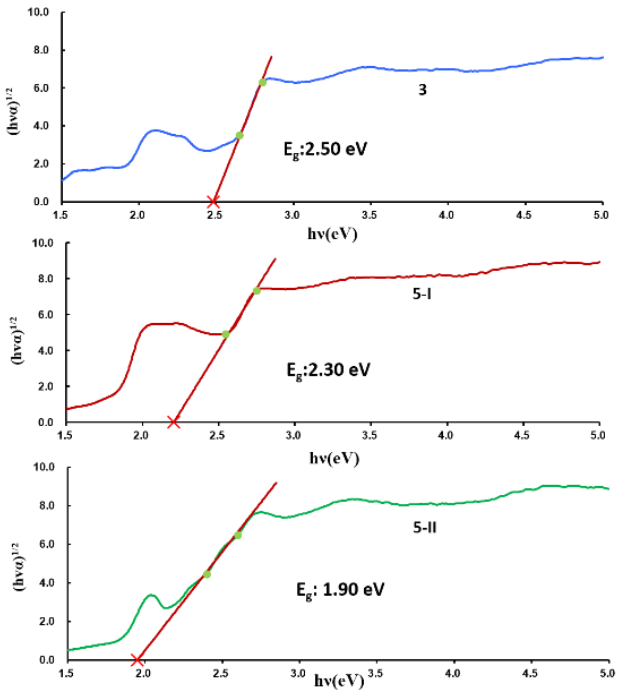

Figure 14. The indirect bandgap measurement of **3, 5-I** and **5-II** via Tauc plotting of the DRS spectra in crystalline state

Conclusions

In summary, we have successfully designed and executed first halogen-bonded BODIPY frameworks architecture. The halogen bond formation was investigated by experimental characterization and theoretical calculations. Despite the fact that all studied molecules **2-5-I** and **5-II** possess large σ–holes on **X** (**Br**, **I**) and a strong Lewis base (**-NO_2**) in their structures, **2** and **4** are not capable of forming XBs due to possible competition of other non-covalent interactions (HB and F···π). However, introducing a second halogen substituent in **3** and **5** has led to the strengthening of σ–holes in these compounds thus enabling the formation of halogen bonds. The decomposition of halogen binding energies performed using SAPT procedure, has revealed that the dispersion forces dominate in these interactions. This indicated that iodine-containing XB are stronger than bromine-containing ones. Different crystallization conditions allowed the stabilization of two polymorphs of compound **5**, as evidenced from single crystal X-ray structures of **5-I** and **5-II**. The structural and electronic features of **5-II** differ from isostructural **3** and **5-I**. The BODIPY core in **5-II** is practically planar while geometry deformation is observed in **3** and **5-I**. Moreover, the rotation of meso-phenyl group with respect to boron-dipyrromethene plane is different between **5-II** and **3, 5-I**. In crystal state the compounds **2, 3, 4**, **5-I** form dimers through CH···F hydrogen bonds. However, the molecular dimers in **2** and **4** are extended into 1D chains *via* CH···F and HB, while the dimers of **3, 5-I** are joined to form 1D tubular structure in the crystal by halogen bonds. In the crystal of **5-II** the molecules are joined by the bifurcated nearly symmetrical XB forming the 1D zig zag chains.

All studied compounds exhibit very weak emission in disordered states (solution, amorphous) mainly due to heavy atom effect and other non-radiative decay process. Surprisingly, crystalline **5-II** exhibit intense fluorescence emission, whereas crystalline **2**-**5-I** show weak emissions in solid state. The halogen bonding present in crystals of **3**, **5-I** and **5-II** leads to delocalization between oxygen and halogen atom and enhances both singlet-to-triplet intersystem crossing (ISC) and triplet-to-singlet reverse intersystem crossing (rISC) to activate fluorescence emission. The indirect optical band gaps of the **3**, **5-I** and **5-II** were tunable in the range of **1.9**–**2.50** eV via XB driven crystal packings. The calculation of LOLIPOP has revealed that XB has led to strong π-delocalization of BODIPY core in order **5-II**>**5-I**>**3** which is in agreement with the observed IR, absorbance, fluorescence and optical bandgap spectral features. In addition, while the XBs induce delocalization through BODIPY core favoring fluorescence emission, dihedral angle of meso-phenyl group and BODIPY core deformation cause non-radiative decay of emission. The combination of these factors may be the reason for strong emission of **5-II** and weak emissions of **3** and **5-I** in crystalline state. We believe that these findings will prove to be of key importance for the future rational design of complex organic electronic materials.

Conflicts of interest

There are no conflicts of interest to declare.

Acknowledgements

The authors thank the TUBITAK ULAKBIM High Performance and Grid Computing Center (TRUBA resources), Turkey, for computational facilities.

Notes and references

1 C. Staudinger, J. Breininger, I. Klimant and S. M. Borisov, *Analyst*, 2019, **144**, 2393–2402.
2 D. Pfeifer, A. Russegger, I. Klimant and S. M. Borisov, *Sensors Actuators, B Chem.*, 2020, **304**, 127312.
3 S. Kolemen, O. A. Bozdemir, Y. Cakmak, G. Barin, S. Erten-Ela, M. Marszalek, J. H. Yum, S. M. Zakeeruddin, M. K. Nazeeruddin, M. Grätzel and E. U. Akkaya, *Chem. Sci.*, 2011, **2**, 949–954.
4 A. Kamkaew, S. H. Lim, H. B. Lee, L. V. Kiew, L. Y. Chung and K. Burgess, *Chem. Soc. Rev.*, 2013, **42**, 77–88.
5 J. Zou, Z. Yin, P. Wang, D. Chen, J. Shao, Q. Zhang, L. Sun, W. Huang and X. Dong, *Chem. Sci.*, 2018, **9**, 2188–2194.
6 M. Ozdemir, D. Choi, Y. Zorlu, B. Cosut, H. Kim, C. Kim and H. Usta, *New J. Chem.*, 2017, **41**, 6232–6240.
7 D. A. Merkushev, S. D. Usoltsev, Y. S. Marfin, A. P. Pushkarev, D. Volyniuk, J. V. Grazulevicius and E. V. Rumyantsev, *Mater. Chem. Phys.*, 2017, **187**, 104–111.
8 Z. Liu, Z. Jiang, M. Yan and X. Wang, *Front. Chem.*, 2019, **7**, 1–16.
9 M. Yamaguchi, S. Ito, A. Hirose, K. Tanaka and Y. Chujo, *Mater. Chem. Front.*, 2017, **1**, 1573–1579.
10 C. L. Liu, Y. Chen, D. P. Shelar, C. Li, G. Cheng and W. F. Fu, *J. Mater. Chem. C*, 2014, **2**, 5471–5478.
11 S. Kim, J. Bouffard and Y. Kim, *Chem. - A Eur. J.*, 2015, **21**, 17459–17465.
12 C. Spies, A. M. Huynh, V. Huch and G. Jung, *J. Phys. Chem. C*, 2013, **117**, 18163–18169.
13 S. Choi, J. Bouffard and Y. Kim, *Chem. Sci.*, 2014, **5**, 751–755.
14 D. Tian, F. Qi, H. Ma, X. Wang, Y. Pan, R. Chen, Z. Shen, Z. Liu, L. Huang and W. Huang, *Nat. Commun.*, 2018, **9**, 1–9.
15 D. Avobenzone, G. Zhang, J. Lu, M. Sabat and C. L. Fraser, *J. Am. Chem. Soc.*, 2010, **132**, 2160–2162.
16 X. He, A. C. Benniston, H. Saarenpää, H. Lemmetyinen, N. V. Tkachenko and U. Baisch, *Chem. Sci.*, 2015, **6**, 3525–3532.
17 D. Yan and D. G. Evans, *Mater. Horizons*, 2014, **1**, 46–57.
18 T. Mutai, H. Tomoda, T. Ohkawa, Y. Yabe and K. Araki, *Angew. Chemie - Int. Ed.*, 2008, **47**, 9522–9524.
19 J. Cao, X. Yan, W. He, X. Li, Z. Li, Y. Mo, M. Liu and Y. B. Jiang, *J. Am. Chem. Soc.*, 2017, **139**, 6605–6610.
20 J. Dahlke, R. Tepper, R. Geitner, S. Zechel, J. Vitz, R. Kampes, J. Popp, M. D. Hager and U. S. Schubert, *Polym. Chem.*, 2018, **9**, 2193–2197.
21 M. Saccone, G. Cavallo, P. Metrangolo, G. Resnati and A. Priimagi, *Top. Curr. Chem.*, 2014, **359**, 147–166.
22 P. Auffinger, F. A. Hays, E. Westhof and P. S. Ho, *Proc. Natl. Acad. Sci. U. S. A.*, 2004, **101**, 16789–94.
23 L. C. Gilday, S. W. Robinson, T. A. Barendt, M. J. Langton, B. R. Mullaney and P. D. Beer, *Chem. Rev.*, 2015, **115**, 7118–7195.
24 G. R. Desiraju, P. S. Ho, L. Kloo, A. C. Legon, R. Marquardt, P. Metrangolo, P. Politzer, G. Resnati and K. Rissanen, *Pure Appl. Chem.*, 2013, **85**, 1711–1713.
25 Ö. D. Ateş, Y. Zorlu, S. D. Kanmazalp, Y. Chumakov, A. G. Gürek and M. M. Ayhan, *CrystEngComm*, 2018, **20**, 3858–3867.
26 O. Bolton, K. Lee, H. J. Kim, K. Y. Lin and J. Kim, *Nat. Chem.*, 2011, **3**, 205–210.
27 J. K. Salunke, N. A. Durandin, T. P. Ruoko, N. R. Candeias, P. Vivo, E. Vuorimaa-Laukkanen, T. Laaksonen and A. Priimagi, *Sci. Rep.*, 2018, **8**, 1–8.
28 S. J. Ang, T. S. Chwee and M. W. Wong, *J. Phys. Chem. C*, 2018, **122**, 12441–12447.
29 L. Xiao, Y. Wu, J. Chen, Z. Yu, Y. Liu, J. Yao and H. Fu, *J. Phys. Chem. A*, 2017, **121**, 8652–8658.
30 D. Yan, A. Delori, G. O. Lloyd, T. Friščić, G. M. Day, W. Jones, J. Lu, M. Wei, D. G. Evans and X. Duan, *Angew. Chemie - Int. Ed.*, 2011, **50**, 12483–12486.
31 V. Kumar, T. Pilati, G. Terraneo, F. Meyer, P. Metrangolo and G. Resnati, *Chem. Sci.*, 2017, **8**, 1801–1810.
32 N. Ramasubbu, R. Parthasarathy and P. Murray-Rust, *J. Am. Chem. Soc.*, 1986, **108**, 4308–4314.
33 K. Raatikainen, M. Cametti and K. Rissanen, *Beilstein J. Org. Chem.*, 2010, **6**, 1–13.
34 B. Ji, W. Wang, D. Deng and Y. Zhang, *Cryst. Growth Des.*, 2011, **11**, 3622–3628.
35 M. J. Frisch, G. W. Trucks, H. B. Schlegel, G. E. Scuseria, M. A. Robb, J. R. Cheeseman, G. Scalmani, B. M. V. Barone, G. A. Petersson and H. Nakatsuji, 2010.
36 J. F. Gonthier, S. N. Steinmann, L. Roch, A. Ruggi, N. Luisier, K. Severin and C. Corminboeuf, *Chem. Commun.*, 2012, **48**, 9239–9241.
37 B. Jeziorski, R. Moszynski and K. Szalewicz, *Chem. Rev.*, 1994, **94**, 1887–1930.
38 T. Korona, R. Moszynski and B. Jeziorski, *J. Chem. Phys.*, 1996, **105**, 8178–8186.
39 K. Szalewicz, *Wiley Interdiscip. Rev. Comput. Mol. Sci.*, 2012, **2**, 254–272.
40 D. Aydin Tekdaş, G. Viswanathan, S. Zehra Topal, C. Y. Looi, W. F. Wong, G. Min Yi Tan, Y. Zorlu, A. G. Gürek, H. B. Lee and F. Dumoulin, *Org. Biomol. Chem.*, 2016, **14**, 2665–2670.
41 L. Wang, K. Q. Zhu, Q. Chen and M. Y. He, *Dye. Pigment.*, 2015, **112**, 274–279.
42 J. H. Ye, Z. Hu, Y. Wang, W. Zhang and Y. Zhang, *Tetrahedron Lett.*, 2012, **53**, 6858–6860.
43 APEX2. Ver. 2014.11-0, Bruker, 2014.
44 SAINT, version 8.34A, Bruker, Bruker AXS Inc., Madison, 2013.

45 SADABS, version2014/5, Bruker, Bruker AXS Inc., Madison, 2014.
46 G. M. Sheldrick, *Acta Crystallogr. Sect. C Struct. Chem.*, 2015, **71**, 3–8.
47 O. V. Dolomanov, L. J. Bourhis, R. J. Gildea, J. A. K. Howard and H. Puschmann, *J. Appl. Crystallogr.*, 2009, **42**, 339–341.
48 A. L. Spek, *Acta Crystallogr. Sect. D Biol. Crystallogr.*, 2009, **65**, 148–155.
49 A. Bondi, *J. Phys. Chem.*, 1964, **68**, 441–451.
50 C. F. Macrae, P. R. Edgington, P. McCabe, E. Pidcock, G. P. Shields, R. Taylor, M. Towler and J. Van De Streek, *J. Appl. Crystallogr.*, 2006, **39**, 453–457.
51 T. M. Krygowski, *J. Chem. Inf. Comput. Sci.*, 1993, **33**, 70–78.
52 T. Lu and F. Chen, *J. Comput. Chem.*, 2012, **33**, 580–592.
53 H. L. Schmider and A. D. Becke, *J. Mol. Struct. THEOCHEM*, 2000, **527**, 51–61.
54 S. N. Steinmann, Y. Mo and C. Corminboeuf, *Phys. Chem. Chem. Phys.*, 2011, **13**, 20584–20592.
55 J. M. Turney, A. C. Simmonett, R. M. Parrish, E. G. Hohenstein, F. A. Evangelista, J. T. Fermann, B. J. Mintz, L. A. Burns, J. J. Wilke, M. L. Abrams, N. J. Russ, M. L. Leininger, C. L. Janssen, E. T. Seidl, W. D. Allen, H. F. Schaefer, R. A. King, E. F. Valeev, C. D. Sherrill and T. D. Crawford, *Wiley Interdiscip. Rev. Comput. Mol. Sci.*, 2012, **2**, 556–565.
56 N. R. Goud, O. Bolton, E. C. Burgess and A. J. Matzger, *Cryst. Growth Des.*, 2016, **16**, 1765–1771.
57 S. Tothadi, P. Sanphui and G. R. Desiraju, *Cryst. Growth Des.*, 2014, **14**, 5293–5302.
58 J. C. Bennion, L. Vogt, M. E. Tuckerman and A. J. Matzger, *Cryst. Growth Des.*, 2016, **16**, 4688–4693.
59 A. Ebrahimi, H. Razmazma and H. S. Delarami, , DOI:10.22036/pcr.2016.11619.
60 L. C. Gilday, S. W. Robinson, T. A. Barendt, M. J. Langton, B. R. Mullaney and P. D. Beer, *Chem. Rev.*, 2015, **115**, 7118–7195.
61 A. R. Voth, P. Khuu, K. Oishi and P. S. Ho, *Nat. Chem.*, 2009, **1**, 74–79.
62 C. R. Groom, I. J. Bruno, M. P. Lightfoot and S. C. Ward, *Acta Crystallogr. Sect. B Struct. Sci. Cryst. Eng. Mater.*, 2016, **72**, 171–179.
63 G.-G. Luo, J.-X. Xia, K. Fang, Q.-H. Zhao, J. Wu and J.-C. Dai, *Dalt. Trans.*, 2013, **42**, 16268–1671.
64 X. Ma, K. Cai and J. Wang, *J. Phys. Chem. B*, 2011, **115**, 1175–1187.
65 Q. Jin Shen and W. Jun Jin, *Phys. Chem. Chem. Phys.*, 2011, **13**, 13721–13729.
66 J. Karolin, L. B. A. Johansson, L. Strandberg and T. Ny, *J. Am. Chem. Soc.*, 1994, **116**, 7801–7806.
67 J. Tian, J. Zhou, Z. Shen, L. Ding, J. S. Yu and H. Ju, *Chem. Sci.*, 2015, **6**, 5969–5977.
68 Y. P. Rey, D. G. Abradelo, N. Santschi, C. A. Strassert and R. Gilmour, *European J. Org. Chem.*, 2017, **2017**, 2170–2178.
69 A. Gorman, J. Killoran, C. O'Shea, T. Kenna, W. M. Gallagher and D. F. O'Shea, *J. Am. Chem. Soc.*, 2004, **126**, 10619–10631.
70 X. Miao, W. Hu, T. He, H. Tao, Q. Wang, R. Chen, L. Jin, H. Zhao, X. Lu, Q. Fan and W. Huang, *Chem. Sci.*, 2019, **10**, 3096–3102.
71 Q. J. Hu, Y. C. Lu, C. X. Yang and X. P. Yan, *Chem. Commun.*, 2016, **52**, 5470–5473.
72 Z. Lou, Y. Hou, K. Chen, J. Zhao, S. Ji, F. Zhong, Y. Dede and B. Dick, *J. Phys. Chem. C*, 2018, **122**, 185–193.
73 Y. Kubota, J. Uehara, K. Funabiki, M. Ebihara and M. Matsui, *Tetrahedron Lett.*, 2010, **51**, 6195–6198.
74 J. Tauc, R. Grigorovici and A. Vancu, *phys. stat. sol.*, 1966, **15**, 625–637.
75 J. Tauc, *Optical Properties of Solids*, Abeles, North Holland, Amsterdam, 1972.
76 N. F. Mott and E. A. Davis, *Philos. Mag.*, 1970, **22**, 903–922.